A new structure of Tesla coupled nozzle in synthetic jet micro-pump

Canh-Dung Tran[1], Pham Hong Phuc[2], Tuan-Khoa Nguyen[3], Hoang-Phuong Phan[3], Toan Dinh[1], Thanh Viet Nguyen[4], Tung Thanh Bui[5], Chu Duc Trinh[5], Nam-Trung Nguyen[3], Dzung Viet Dao[4] and Van Thanh Dau[4]*

[1] *School of Mechanical and Electrical Engineering, University of Southern Queensland, Australia*
[2] *Hanoi University of Science and Technology, Hanoi, Viet Nam*
[3] *Queensland Micro and Nanotechnology Centre, Griffith University, Queensland, Australia*
[4] *School of Engineering and Built Environment, Griffith University, Queensland, Australia*
[5] *VNU University of Engineering and Technology, Hanoi Viet Nam*

[*] *E-mail: v.dau@griffith.edu.au*

Abstract

Synthetic jet pump is a potential technique to improve the pumping performance by introducing a smart structure which can enhance counter-rotating vortexes. Aligning with this approach, a new structure of valveless micro-pump is developed in this work. The mechanism of the present micro-pump is based on the combination of the nozzle and a tesla element to rectify the synthetic jet. The new structure of "ace of spades" nozzle, named Tesla coupled nozzle, create series of vortexes at the orifice of the pump chamber that allows to attenuate and/or block reversed flows while fluid is drawn through the pump. The present micro-pump is simple but robust and can perform at rather low voltages.

1. Introduction

Flow in a micro-pump can be rectified by either a valve or valveless structure. Valveless pumps with simple structures in general, do not include any moving part. Valveless pumps generate flow by either a non-mechanical or mechanical actuator [1]. This approach can be classified in two categories. In the first category, micro-pumps are based on the mechanical displacement and use rectifying diffuser-nozzle structures, where the converging and diverging parts generate different flow resistances. For this approach, the flow rectification can be carried by either adjusting several liquid properties (e.g. the viscosity) [2] or using different rectification structures [3]. On the later technique, several structures have been developed, including the diffuser-nozzle element [4–7], Tesla element [8–10], recirculation vortex channel [11] and bifurcated channel [12]. The diffuser and nozzle are not directly connected each other, but they are linked to a pump chamber at two separated positions. This category is popularly presented in the literature. Numerous experimental and numerical studies on the flow in diffuser-nozzle structures showed that the efficiency of such valveless micro-pumps depends on both the structural geometry and the liquid properties. Singhal *et al.* [13] found that the rectification of gradually expanded conical and planar diffusers is significantly improved with increasing the Reynolds number. In addition, the Reynold number significantly affects the characteristics of fluid flows through a nozzle [14]. Several numerical and experimental optimizations were carried out to improve the efficiency of diffuser-nozzle structures by the geometrical tuning [15,16].

On the other hand, the second category, the synthetic jet technique, has been used to rectify fluid flow by a chain of vortexes [17][18]. In this technique, flow in a valveless pump is basically generated by the interaction of the pairs of counter-rotating vortexes at the edge of an orifice. This is created by an oscillating diaphragm which is installed in a sealed cavity [19–23]. Such system includes a pump chamber which is sealed at one side and linked to an emitting nozzle at another one. Thus, no diffuser is required. A modification of this technique using the Coanda effect was recently reported by Song *et al.* [24] and He *et al*. [25]. Finally, based on the working principle of a chain of vortexes, many design variants, for example, the combination of diffuser-nozzle or fluidic diode with the synthetic jet [26] [27], batwing-junction [28], T-junction [29], internal vortex membrane [30] were successfully applied in droplet forming, pinching, circulating or simultaneously pumping and mixing.

Thus, it is reasonable to assume that the synthetic jet is a potential technique for improving the pumping performance by a smart structure which can enhance counter-rotating vortexes. This approach yields stronger vortexes and consequently better flow rectification. In this spirit, this work reports for the first time a structure of "ace of spades" nozzle which is implemented in a valveless micro-pump. The present technique is based on the combination of the nozzle-diffuser and a Tesla element to rectify the synthetic jet. The new structure called Tesla coupled nozzle (TCN) enhances the rectifying effect owing to a created side channel that can attenuate and/or block the reversed flow while the chamber draws liquid into the pump. The present micro-pump is simple but mechanically robust, has quick response time and yields a significant improvement of the pumping performance.

2. DESIGN OF PRESENT PUMP

2.1. MECHANISM OF PUMP

Fig. 1(a) describes a schema of the micro-pump with TCN structure and its 3D-planar prototype. A piezoelectric lead zirconate titanate (PZT) diaphragm (ordered from Murata Ltd. and several specifications are mention below), actuated by an external voltage, deforms with the voltage polarity (1). Since the rim of the diaphragm is rigidly fixed, it primarily vibrates on the vertical direction perpendicular to the radial direction of diaphragm. The vibrating diaphragm (1) introduces liquid into the pump chamber (2) which is connected to the outlet (4) through a chamber-inlet junction (5). The junction is a valveless structure consisting of a nozzle-diffuser coupled with an element whose operation is inspired from Tesla principle to prevent the undesired backflow (see Fig. 1(b)).

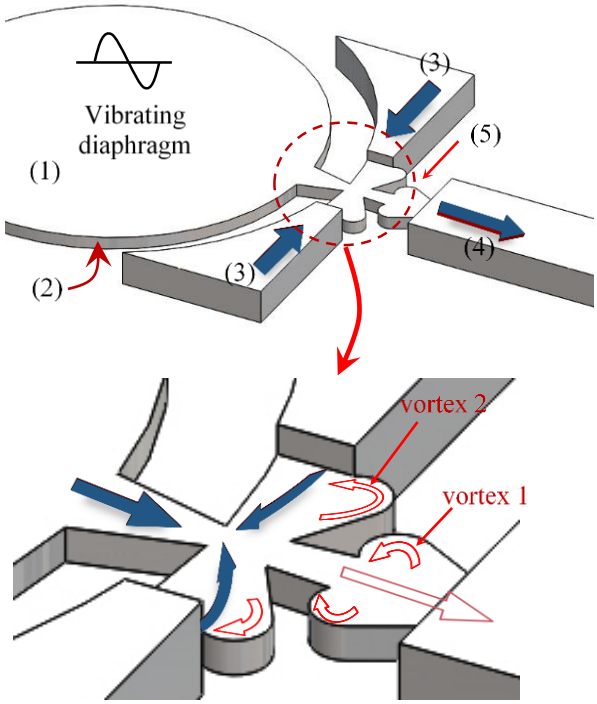

Figure 1. *(above) A schema of device with TCN of "ace of spades" structure of the 3D-planar model: (1) diaphragm; (2) pump chamber; (3) inflow; (4) outflow and (5) TCN; and (below) the outflow rectified by vortexes in two pairs of spades of the TCN when diaphragm vibrates to generate synthetic jet.*

The operation of the micro-pump consists of the charge and discharge phases. In the charge phase, liquid is sucked into the pump chamber by the up moving diaphragm while the down moving diaphragm pushes liquid out of the chamber in the discharge phase.

In both phases, liquid moves through the TCN and the flow is then rectified. During the discharge phase, the TCN ensures liquid leaves the pump chamber with a high velocity, then moves straight into the outlet channel to form the first vortexes (1) in the pair of small spades/cavities of the TCN due to its high speed. Meanwhile, a small portion of liquid that does not move into the outlet channel creates the second vortexes (2) as the liquid flows along the curved wall of the pair of bigger spades of the Tesla element, known as the Coanda effect [31], and then moves back to the central of nozzle (see Fig. 1(b)). Thus, the Tesla element is set up at the downstream of the nozzle and the inlet channel to enhance the rectification of the liquid flow.

After the first pumping cycle, the vortices (2) increase the velocity of liquid sucked into the pump chamber from the inlet during the charge phase, whereas the vortices (1) block the backward motion of liquid from the outlet during the discharge phase. In other words, the backflow from the outlet of the charge phase slows down and is interrupted by the inflow from the inlet. The vortices in spades of TCN become stronger due to the momentum accumulated by the diaphragm vibration, which boosts the rectifying effect to create a jet flow in the outlet channel.

The above 3D-planar model has been expanded into the 3D-axisymmetric prototype, which is easily fabricated using either the laser machining or the 3D printing technique. In our experiments,

the 3D-planar model was designed with a depth of 1 mm at the nozzle, while the 3D-axisymmetric prototype was a cylindrical structure with a radius of 0.6 mm. Other dimensions are detailed in Fig. 4). Furthermore, PZT diaphragm by Murata Ltd. of 20 mm diameter was used for both models and the rim of PZT diaphragm is fixed using epoxy glue.

2.2. SIMULATION OF PRESENT PUMP'S OPERATION

In this work, ethanol was used as the working fluid and the operation of the present device is numerically simulated. The transient flow is described by the Navier–Stokes equation for a laminar and incompressible fluid as follows

$$\nabla \cdot \vec{u} = 0 \tag{1}$$

$$\frac{\partial \vec{u}}{\partial t} + (\vec{u} \cdot \nabla)\vec{u} = \frac{\nabla p}{\rho} + (\eta \nabla \vec{u}) \tag{2}$$

The boundary condition at time steps ($t = 0$ is for the initial condition) imposed on the diaphragm is converted from its vibrating velocity $v(\vec{r}, t)$ into the shape function $\varphi(r)$, which is applicable for both the 2D and the axisymmetric models as:

$$v(\vec{r}, t) = 2\pi f Z \cos(2\pi f t)\, \varphi(\vec{r}), \tag{3}$$

where $\varphi(r) = (1 - (r/a)^2)^2$ is the shape function of a circular diaphragm under an uniform load [32] and a is the diaphragm radius of 10 mm in this work.

Solving Eqs. (1)-(2) with the boundary condition given by Eq. (3) for each mesh grid in the ANSYS/FLUENT environment results in the pressure and velocity fields in the device. We utilized the hybrid of the Pressure-Implicit with Splitting (PISO) scheme and the Semi-Implicit Method for Pressure Linked Equation (SIMPLE) as the velocity–pressure coupling algorithm.

By this numerical method, the calculation was advanced with time by the implicit second-order scheme. The PZT diaphragm, whose boundary condition is described by Eq. (3), was considered as the inlet condition. For the numerical stability, the time step was chosen as one-fortieth of the vibration period of the PZT diaphragm. Fig. 2 (a)&(b) illustrates the geometry of two 3D models. Figure 2a shows the representative mesh of the 3D-planar model together with the displacement of the diaphragm. Figures 2(c)&(d) show the representative streamlines of the velocity fields in the charge and discharge phases of the micro-pump, confirming the working principle of the TCN where large vortices rectify the flow direction from the inlet to the outlet.

Similar to the description in section 2.1, the numerical simulation by Fig. 2 also shows that vortexes are formed in both small and large spades of Tesla element by either high speed flow through the TCN (vortex 1, Fig. 1(b) & Fig. 2(c,d)) or a partial liquid moving along the curved wall (vortex 2, Fig. 1(b)& Fig. 2(c,d)). These vortexes rotate in the same CCW direction during both charge and discharge phases, when liquid flows forth and back through the nozzle junction, thus enhancing the rectification of flow.

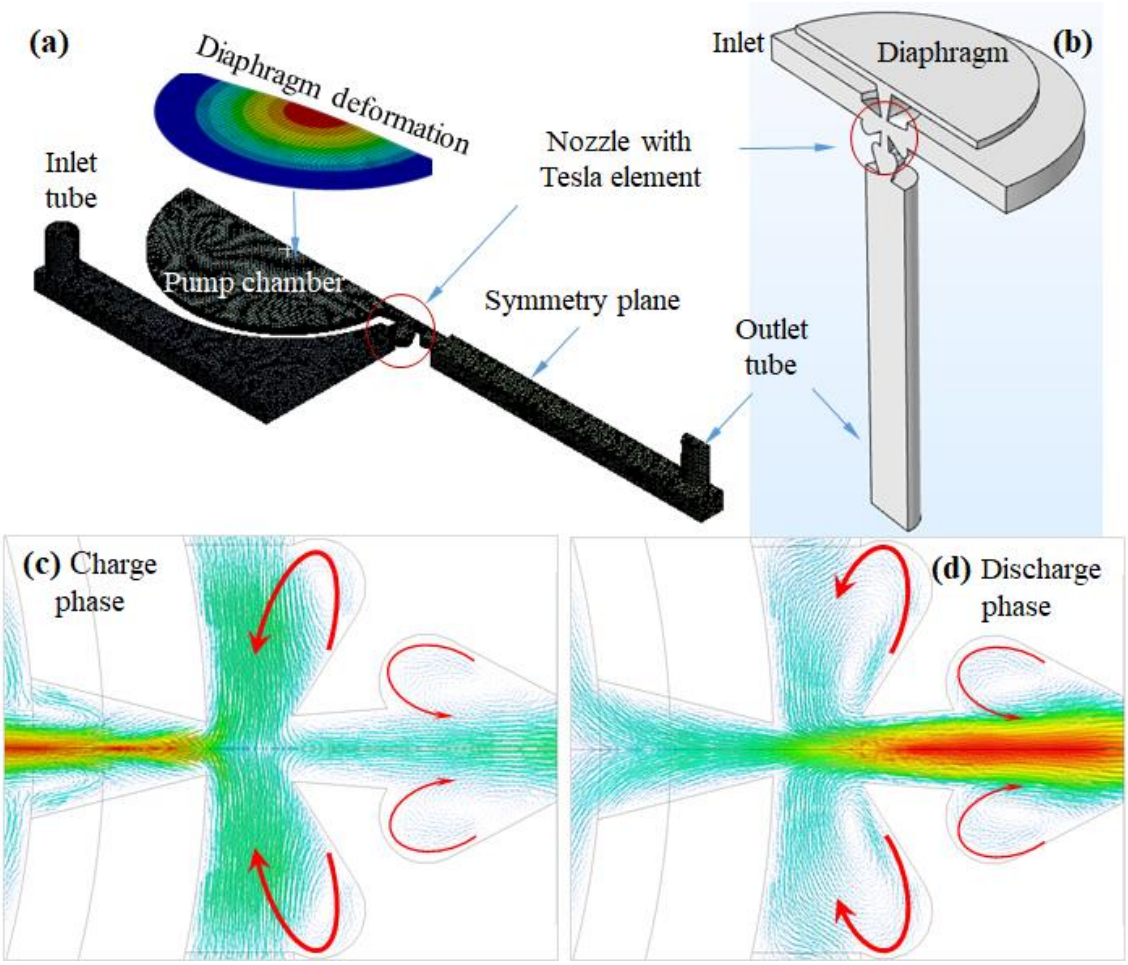

Figure 2*: Simulation of the pumping device. (a) TCN structure in 3D-planar model: displacement contours of the diaphragm (Fig. 2a-Upper figure) and meshing of the present device (Fig. 2a-Lower figure); (b) TCN structure in 3D- axisymmetric model; and (c)&(d) streamlines of the velocity field of flow at the TCN of the planar model for the charge and discharge phases of the device, respectively: red arrows show the direction of vortexes to enhance the flow rectification.*

Figure 3 presents the simulated time-dependent flowrate at the outlet through the TCN during two phases for both planar and axisymmetric models. It is worth noting that a positive average flowrate at the outlet means a flow from the inlet moving into the device.

The results by Fig. 3 clearly show that the backflow of the 3D-planar model is eliminated during the discharge phase after few operation cycles as the flowrate curve quickly shifts above the x-axis (solid line in Fig. 3). That validates the working principle of the present device as elaborated in Section 2.1. For the 3D-axisymmetric model, although the flowrate is always positive at both the outlet and inlet for an operation cycle (red dot line in Fig.3), the net flow unidirectionally moves through the pump. Furthermore, results also predict that the asymmetric model rectifies more efficiently as its flowrate curve is much higher than that of the planar model in both charge and discharge phases. This is from the different structures of two models. In fact, vortexes created within larger and smooth cavities of the axisymmetric model based TCN are much stronger (in terms of

the velocity and momentum) than those by the planar model, yielding a higher efficiency of the flow rectification.

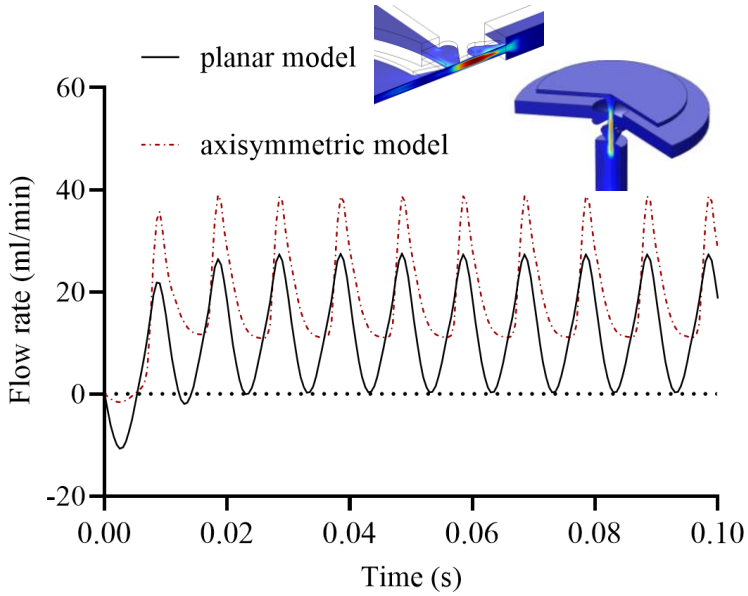

***Figure 3**: Simulating results of the 3D-planar and 3D-axisymmetric models: instantaneous flowrate at the outlet of the present pumps in the 3D-planar and 3D-axisymmetric models. The pumping frequency is f = 100 Hz.*

3. EXPERIMENT

The prototypes of the present valveless micro-pump corresponding the 3D-planar and 3D-axisymmetric models produced using the 3D printing system of Conex3 Objet500, Stratasys are shown in Figures 4c and b, respectively. Figure 4c also shows a cross-section of the Tesla element.

A programmable generator (Hameg HM 8131-2) generates a sinusoidal voltage, which is then amplified by an AC voltage amplifier for driving the PZT diaphragm. The flowrate at zero-backpressure was calibrated by adjusting the liquid amount pumped through the outlet, while the device is set up on the horizontal direction. The backpressure was measured by connecting the outlet with a glass tube and observing the liquid height. The effect of backpressure on flow rate is determined by monitoring the pumped liquid rate in this glass tube at each level of liquid height.

For the sake of our easy experiment, ethanol was used as the working liquid of micro-pump because of its low surface tension, which allows to easily detect the liquid leakage and prevent air bubble blocked at the internal wall of the device. The flowrate at the zero-backpressure is investigated for a range of the driving frequencies of the diaphragm from 0 to 400 Hz; at peak-to-peak driving voltages of V_{pp} = 250V and 150V for the 3D-planar and 3D-axisymmetric models, respectively. The two prototypes were experimentally investigated to evaluate the effects of the driving frequency and voltage on the pump head and flow rates.

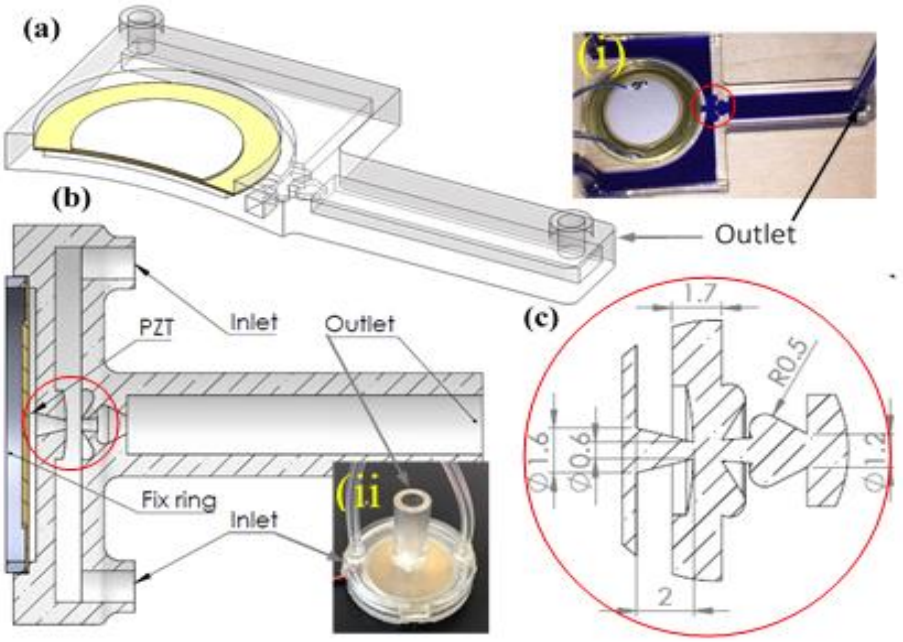

Figure 4*. Model and prototype of the present micro-pump: (a) Model and prototype of the pump designed in 3D-planar model; (b) 3D-axisymmetric model and the corresponding prototype of the present pump; and (c) Cross-section of the Tesla coupled nozzle structure.*

3.1 Effect of the diaphragm frequency

Figure 5 shows the experimental results. Starting from a low driving frequency (nearly 0 Hz), the pumping pressure increases with increasing frequency and reaches a maximum at around 3.95 kPa at a frequency of 310 Hz and a voltage of 250V as well as 4.25 kPa at 330Hz and a voltage of 120V for the 3D-planar and 3D-axisymmetric prototypes, respectively. The pump head then decreases as the frequency is beyond 350 Hz for both cases.

The pump frequency creating a maximum pump head are at the resonant frequency of approximately 310-330 Hz, which are considerably offset from those of the PZT diagphram itself or its air pumping application [33][34]. We discussed that the resonant frequency of a valveless pump mainly depends on the material and geometry of the diaphragm, the pump chamber and the liquid in our recent publication [35]. Through this work, experimental observations found that the converting of Tesla couped nozzle structure from the planar model into the axisymmetric model does not yield a significant change of the resonant frequency of the system. Interestingly, the two peaks in Fig. 5 were reported in literature on the relationship between the formed synthetic jet flow and the resonance jet amplification where the flow rate reaches its highest value [36]. Chiatto et al.[37] stated while considering a single orifice device that the first mode of resonance frequencies is the Helmhotz's frequency, which represents the equivalent stiffness of liquid inside the pump chamber and the effective mass of the liquid at the nozzle, and the second one is natural frequency of the structural oscillator

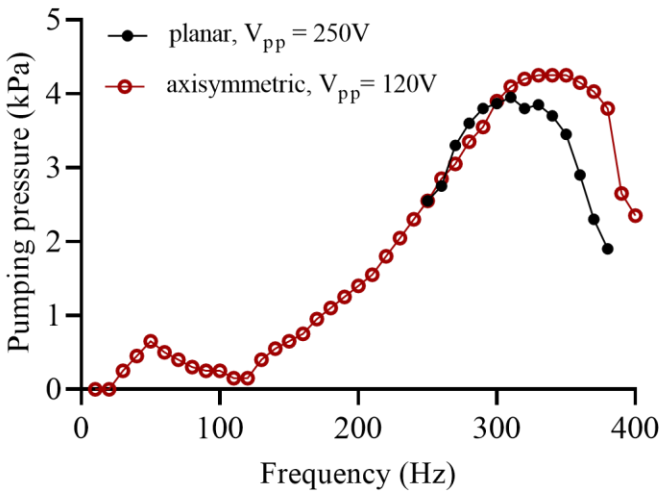

Figure 5*. Experimental results – the effect of the diaphragm frequency on pump head: The liquid level plotted versus the frequency using applied voltages of V_{pzt} = 250V_{pp} and 120V_{pp} to activate the diagraphm vibriation for the planar and axisymmetric models, respectively*

3.2 Effect of the driving voltage V_{pp}

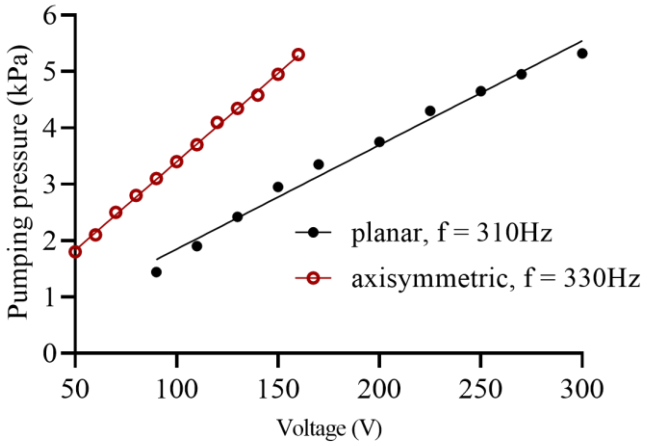

Figure 6*. Experimental results – the effect of the applied voltage on pump head: The liquid height (in mm) plotted versus the driving voltage at the frequencies of 310Hz and 330Hz of diaphragm for the planar and axisymmetric models, respectively.*

Consider the pump head at the resonant frequency of the diaphragm as found in section 3.1 (310Hz and 330Hz for the axisymmetric and planar models, respectively) for a range of applied voltages, results by Fig. 6 show that at a certain voltage, the pump head by the axisymmetric prototype is higher than one by the planar counterpart. Furthermore, while the pump head linearly increases with the increasing voltage for both cases, the axisymmetric prototype provides a higher rate than that of the planar prototype as depicted by the red line in Fig. 6.

For the present valveless structure, experimental results depict that the pumping pressure linearly increases with the driving voltage at a rate of 33.1 Pa/V and has reached 5.3 kPa. It is worth noting that this performance is significantly higher than the commercialized counterparts using PZT diaphragms of the similar size, which were working for a range of flowrates of 3 – 7 ml/min as recently published in [38,39].

The linear relationships of flow-rate and pumping pressure versus voltage were published in several previous articles for the synthetic jet pumping where the synthetic jet is applied in a T-junction geometry [40]. Although experiment results by the present TCN structure are in good agreement with their finding, there exists a slight difference from some other reports for the synthetic jet in free space [41–43]

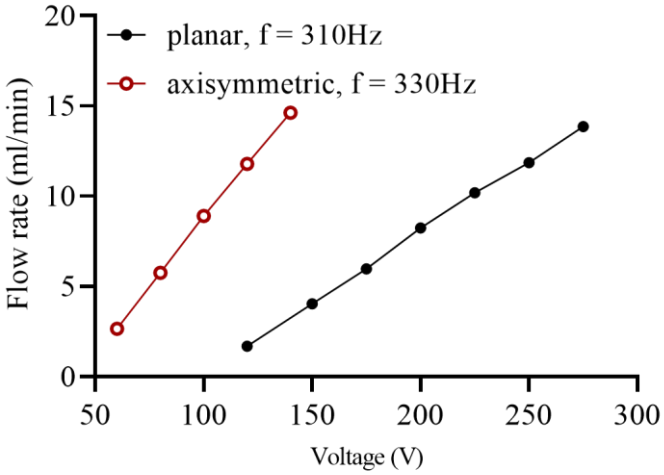

Figure 7. *Experimental results: the flowrate plotted vs the applied voltage at the resonant frequencies of 310Hz and 330Hz of diaphragm for the planar and axisymmetric models, respectively.*

At the resonant frequency (i.e. at the maximum flowrate), the flowrate plotted versus driving voltage applied on the diaphragm V_{pp} (Fig. 7) shows that the higher driving voltage yields a larger diaphragm displacement and consequently a higher flow rate. Specifically, the 3D-planar structure achieves a significant enhancement (in terms of the flow-rate) over those reported in literature using Coanda effect on the order of sub-milliliter per minute at the applied voltage of 360V using PZT diaphragms of the same diameters [24][25] (see also table 1). This evaluation is relative because several parameters of PZT diaphragms used in the citations such as the thickness, diameter and materials which are not disclosed, could be bit different by manufacturers.

Table 1. Flow rate of several valveless pumps using the same class of PZT diaphragms

Valveless pumps	Flow rate (ml/min)
Tesla effect [9]	~ 2.2 ml/min
Bifurcation geometry [12]	~ 0.15 ml/min
Coanda effect [24]	~ 0.22 (ml/min)

Commercial products [38,39]	~ (3 – 7) (ml/min)
This work	~ 15 ml/min

3.3. Effect of backpressure on the pump flowrate

Figure 8 shows the relationship between the flowrate (Q) and the backpressure (P) of our valveless micropump at the resonant frequency and a relatively low voltage of 100V – 150V for the two prototypes. The flowrate linearly decreases with the backpressure with the rate (dQ/dP) of -4.1 (ml/min)kPa^{-1} and -0.58 (ml/min)kPa^{-1} for the axisymmetric and planar models, respectively. The result indicates that the axisymmetric models is seven times as efficient as the planar. This can be explained as the vortex induced by in axisymmetric model are more intense due to smaller flow restriction at the TCN, and as the back pressure rises up, the vortex was forced against its rotation and hence reduces the flowrate of the fluid transported from outlet to inlet.

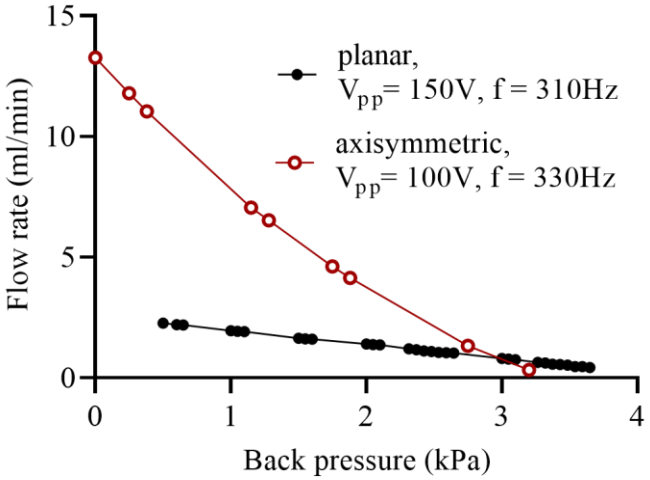

Figure 8*. Experimental results - Effect of backpressure on the flowrate/pump rate: The flowrate plotted versus the backpressure at the resonant frequency for the axisymmetric and planar structures.*

4. Conclusion:

We reported numerical and experimental results of valveless piezoelectric micro-pumps with Tesla element that works based on the principle of a synthetic jet. The 3D-planar and axisymmetric prototypes were designed, modelled, and tested. Experimental results are in good agreement with the numerical data. For the present approach, the device characterized by the linear relationship between its backpressure and flowrate can achieve ~14 ml/min with an applied voltage as moderate as ~100 V_{pp} corresponding to a backpressure of ~5kPa. Thus, for a desired performance, this micro-pump using the present technique can be driven by an affordable applied voltage.

Reference

[1] D.J. Laser, J.G. Santiago, A review of micropumps, J. Micromechanics Microengineering. 14 (2004) R35–R64. https://doi.org/10.1088/0960-1317/14/6/R01.

[2] D.J. Beebe, J. Moore, J.M. Bauer, Q. Yu, R.H. Liu, C. Devadoss, B.H. Jo, Functional hydrogel structures for autonomous ow control inside microfluidic channels, Nature. 404 (2000) 588.

[3] N.-T. Nguyen, X. Huang, T.K. Chuan, MEMS-Micropumps: A Review, J. Fluids Eng. 124 (2002) 384–392. https://doi.org/10.1115/1.1459075.

[4] T. Gerlach, H. Wurmus, Working principle and performance of the dynamic micropump, "Sensors Actuators, A Phys. 50 (1995) 135–140. https://doi.org/10.1016/0924-4247(96)80097-5.

[5] A. Olsson, P. Enoksson, G. Stemme, E. Stemme, Micromachined flat-walled valveless diffuser pumps, J. Microelectromechanical Syst. 6 (1997) 161–166. https://doi.org/10.1109/84.585794.

[6] E. Stemme, G. Stemme, A valveless diffuser/nozzle-based fluid pump, Sensors Actuators A. Phys. 39 (1993) 159–167. https://doi.org/10.1016/0924-4247(93)80213-Z.

[7] N.-T. Nguyen, X. Huang, Miniature valveless pumps based on printed circuit board technique, Sensors Actuators A Phys. 88 (2001) 104–111. https://doi.org/10.1016/S0924-4247(00)00500-8.

[8] C.J. Morris, F.K. Forster, Low-order modeling of resonance for fixed-valve micropumps based on first principles, J. Microelectromechanical Syst. 12 (2003) 325–334. https://doi.org/10.1109/JMEMS.2003.809965.

[9] A.R. Gamboa, C.J. Morris, F.K. Forster, Improvements in Fixed-Valve Micropump Performance Through Shape Optimization of Valves, J. Fluids Eng. 127 (2005) 339. https://doi.org/10.1115/1.1891151.

[10] A. Gaymann, F. Montomoli, M. Pietropaoli, Design for Additive Manufacturing: Valves Without Moving Parts, in: ASME Turbo Expo 2017 Turbomach. Tech. Conf. Expo. GT2017, 2017. https://doi.org/10.1115/GT2017-64872.

[11] I. Izzo, D. Accoto, A. Menciassi, L. Schmitt, P. Dario, Modeling and experimental validation of a piezoelectric micropump with novel no-moving-part valves, Sensors Actuators, A Phys. 133 (2007) 128–140. https://doi.org/10.1016/j.sna.2006.01.049.

[12] A. Fadl, S. Demming, Z. Zhang, S. Büttgenbach, M. Krafczyk, D.M.L. Meyer, A multifunction and bidirectional valve-less rectification micropump based on bifurcation geometry, Microfluid. Nanofluidics. 9 (2010) 267–280. https://doi.org/10.1007/s10404-009-0544-0.

[13] V. Singhal, S. V. Garimella, J.Y. Murthy, Low Reynolds number flow through nozzle-diffuser elements in valveless micropumps, Sensors Actuators, A Phys. 113 (2004) 226–235. https://doi.org/10.1016/j.sna.2004.03.002.

[14] A. Olsson, G. Stemme, E. Stemme, Numerical and experimental studies of flat-walled diffuser elements for valve-less micropumps, Sensors Actuators, A Phys. 84 (2000) 165–175. https://doi.org/10.1016/S0924-4247(99)00320-9.

[15] Y.C. Wang, J.C. Hsu, P.C. Kuo, Y.C. Lee, Loss characteristics and flow rectification property of diffuser valves for micropump applications, Int. J. Heat Mass Transf. 52 (2009) 328–336. https://doi.org/10.1016/j.ijheatmasstransfer.2008.06.010.

[16] A. Chandrasekaran, M. Packirisamy, Improved Efficiency of Microdiffuser Through Geometry Tuning for Valveless Micropumps, J. Fluids Eng. 138 (2015) 031101. https://doi.org/10.1115/1.4031256.

[17] V.T. Dau, T.X. Dinh, T.T. Bui, C.D. Tran, Vortex flow generator utilizing synthetic jets by diaphragm vibration, Int. J. Mech. Sci. 142–143 (2018) 432–439. https://doi.org/10.1016/j.ijmecsci.2018.05.028.

[18] K. Tanaka, V.T. Dau, R. Sakamoto, T.X. Dinh, D.V. Dao, S. Sugiyama, Fabrication and Basic Characterization of a Piezoelectric Valveless Micro Jet Pump, Jpn. J. Appl. Phys. 47 (2008) 8615–8618.

https://doi.org/10.1143/JJAP.47.8615.

[19] B.L. Smith, A. Glezer, The formation and evolution of synthetic jets, Phys. Fluids. 10 (1998) 2281. https://doi.org/10.1063/1.869828.

[20] B.L. Smith, G.W. Swift, A comparison between synthetic jets and continuous jets, Exp. Fluids. 34 (2003) 467–472. https://doi.org/10.1007/s00348-002-0577-6.

[21] N.K. Yamaleev, M.H. Carpenter, A Reduced-Order Model for Efficient Simulation of Synthetic Jet Actuators, NASA Rep. NASA/TM. (2003) 212664.

[22] V.T. Dau, T.X. Dinh, S. Sugiyama, A MEMS-based silicon micropump with intersecting channels and integrated hotwires, J. Micromechanics Microengineering. 19 (2009) 125016. https://doi.org/10.1088/0960-1317/19/12/125016.

[23] V.T. Dau, T.X. Dinh, C.D. Tran, P.N. Bui, D.D. Vien, H.T. Phan, Fluidic mechanism for dual-axis gyroscope, Mech. Syst. Signal Process. 108 (2018) 73–87. https://doi.org/10.1016/j.ymssp.2018.02.017.

[24] S. Yang, X. He, S. Yuan, J. Zhu, Z. Deng, A valveless piezoelectric micropump with a Coanda jet element, Sensors Actuators, A Phys. 230 (2015) 74–82. https://doi.org/10.1016/j.sna.2015.04.016.

[25] X. He, X. Zhang, S. Yang, J. Zhu, J. Yan, Experiment and numerical simulation of a valveless piezoelectric micropump applying Coanda effect, Mech. Ind. 17 (2016) 204. https://doi.org/10.1051/meca/2015070.

[26] S.S. Hsu, Y.J. Chou, Z. Trávníček, C.F. Lin, A.B. Wang, R.H. Yen, Numerical study of nozzle design for the hybrid synthetic jet actuator, Sensors Actuators, A Phys. 232 (2015) 172–182. https://doi.org/10.1016/j.sna.2015.05.018.

[27] J. Kordík, Z. Trávníček, Novel fluidic diode for hybrid synthetic jet actuator, J. Fluids Eng. Trans. ASME. 135 (2013) 1–7. https://doi.org/10.1115/1.4024679.

[28] J. Li, D.A. Barrow, A new droplet-forming fluidic junction for the generation of highly compartmentalised capsules, Lab Chip. 17 (2017) 2873–2881. https://doi.org/10.1039/C7LC00618G.

[29] F. Munas, G. Melroy, C. Abeynayake, H. Chathuranga, R. Amarasinghe, P. Kumarage, V. Dau, D. Dao, Development of PZT Actuated Valveless Micropump, Sensors. 18 (2018) 1302. https://doi.org/10.3390/s18051302.

[30] A.-B. Wang, M.-C. Hsieh, I.-C. Lin, W.-H. Tsai, Membrane micropump, US 8690550, 2014.

[31] I.W. Hunter, Gas Jet Actuator Using Coanda Effect, US Patent US5067509, 1991.

[32] S. Timoshenko, S. Woinowsky-Krieger, Theory of Plate and Shells, 2nd ed., McGraw-Hill, New York, NY, USA, 1959.

[33] V.T. Dau, T.X. Dinh, Numerical study and experimental validation of a valveless piezoelectric air blower for fluidic applications, Sensors Actuators B Chem. 221 (2015) 1077–1083. https://doi.org/10.1016/j.snb.2015.07.041.

[34] A. Hirata, G. Kamitani, H. Wada, M. Sugana, S. Kanai, Piezoelectric Micro-blower, US 8678787B2, 2014.

[35] L. Le Van, T.T. Bui, C.N. Nhu, A.N. Ngoc, T.X. Dinh, L.B. Dang, C.-D. Tran, T.C. Duc, V.T. Dau, Simulation and Experimental Study of a Synthetic Jet Valveless Pump, IEEE/ASME Trans. Mechatronics. 25 (2020) 1162–1170. https://doi.org/10.1109/TMECH.2019.2960332.

[36] L. de Luca, M. Girfoglio, M. Chiatto, G. Coppola, Scaling properties of resonant cavities driven by piezo-electric actuators, Sensors Actuators, A Phys. 247 (2016) 465–474. https://doi.org/10.1016/j.sna.2016.06.016.

[37] M. Chiatto, A. Palumbo, L. de Luca, Design approach to predict synthetic jet formation and resonance amplifications, Exp. Therm. Fluid Sci. 107 (2019) 79–87. https://doi.org/10.1016/j.expthermflusci.2019.05.013.

[38] Takasago Fluidic Systems, Piezoelectric Micro Pumps SDMP_D Series - Takasago Fluidic Systems, (2019).

[39] Curie Jet Micropump, CurieJet® Liquid/Gas Micro Pump, (2019).

[40] T.X. Dinh, N.T.M. Le, V.T. Dau, Y. Ogami, A dynamic model for studying valveless electromagnetic micropumps, J. Micromechanics Microengineering. 21 (2011) 025015. https://doi.org/10.1088/0960-1317/21/2/025015.

[41] M. Chiatto, F. Capuano, G. Coppola, L. De Luca, LEM Characterization of Synthetic Jet Actuators Driven by Piezoelectric Element: A Review, Sensors. 17 (2017) 1216. https://doi.org/10.3390/s17061216.

[42] W.J. Crowther, L.T. Gomes, An evaluation of the mass and power scaling of synthetic jet actuator flow control technology for civil transport aircraft applications, Proc. Inst. Mech. Eng. Part I J. Syst. Control Eng. 222 (2008) 357–372. https://doi.org/10.1243/09596518JSCE519.

[43] G. Krishnan, K. Mohseni, Axisymmetric Synthetic Jets: An Experimental and Theoretical Examination, AIAA J. 47 (2009) 2273–2283. https://doi.org/10.2514/1.42967.